

Deep Residual Learning for Compressed Sensing CT Reconstruction via Persistent Homology Analysis

Yo Seob Han, Jaejun Yoo and Jong Chul Ye

Bio Imaging Signal Processing Lab

Korea Ad. Inst. of Science & Technology (KAIST)

291 Daehak-ro, Yuseong-gu, Daejeon 34141, Korea

{hanyoseob, jaejun2004, jong.ye}@kaist.ac.kr

Abstract

Recently, compressed sensing (CS) computed tomography (CT) using sparse projection views has been extensively investigated to reduce the potential risk of radiation to patient. However, due to the insufficient number of projection views, an analytic reconstruction approach results in severe streaking artifacts and CS-based iterative approach is computationally very expensive. To address this issue, here we propose a novel deep residual learning approach for sparse-view CT reconstruction. Specifically, based on a novel persistent homology analysis showing that the manifold of streaking artifacts is topologically simpler than original one, a deep residual learning architecture that estimates the streaking artifacts is developed. Once a streaking artifact image is estimated, an artifact-free image can be obtained by subtracting the streaking artifacts from the input image. Using extensive experiments with real patient data set, we confirm that the proposed residual learning provides significantly better image reconstruction performance with several orders of magnitude faster computational speed.

1. Introduction

Recently, deep learning approaches have achieved tremendous success in classification problems [11] as well as low-level computer vision problems such as segmentation [15], denoising [21], super resolution [10, 16], etc. The theoretical origin of their success has been investigated by a few authors [14, 18], where the exponential expressivity under a given network complexity (in terms of VC dimension [1] or Rademacher complexity [2]) has been attributed to their success.

In medical imaging area, there have been also extensive research activities applying deep learning. However, most of these works are focused on image-based diagnostics, and

their applications to image reconstruction problems such as X-ray computed tomography (CT) reconstruction is relatively less investigated.

In X-ray CT, due to the potential risk of radiation exposure, the main research thrust is to reduce the radiation dose. Among various approaches for low-dose CT, sparse view CT is a recent proposal that reduces the radiation dose by reducing the number of projection views [17]. However, due to the insufficient projection views, standard reconstruction using the filtered back-projection (FBP) algorithm exhibits severe streaking artifacts. Accordingly, researchers have extensively employed compressed sensing approaches [5] that minimize the total variation (TV) or other sparsity-inducing penalties under the data fidelity [17]. These approaches are, however, computationally very expensive due to the repeated applications of projection and back-projection during iterative update steps.

Therefore, the main goal of this paper is to develop a novel deep CNN architecture for sparse view CT reconstruction that outperforms the existing approaches in its computational speed as well as reconstruction quality. However, a direct application of conventional CNN architecture turns out to be inferior, because X-ray CT images have high texture details that are often difficult to estimate from sparse view reconstructions. To address this, we propose a novel *deep residual learning* architecture to learn streaking artifacts. Once the streaking artifacts are estimated, an artifact-free image is then obtained by subtracting the estimated streaking artifacts as shown in Fig. 1.

The proposed deep residual learning is based on our conjecture that streaking artifacts from sparse view CT reconstruction may have simpler topological structure such that learning streaking artifacts is easier than learning the original artifact-free images. To prove this conjecture, we employ a recent computational topology tool called the *persistent homology* [6] to show that the residual manifold is much simpler than the original one. For practical imple-

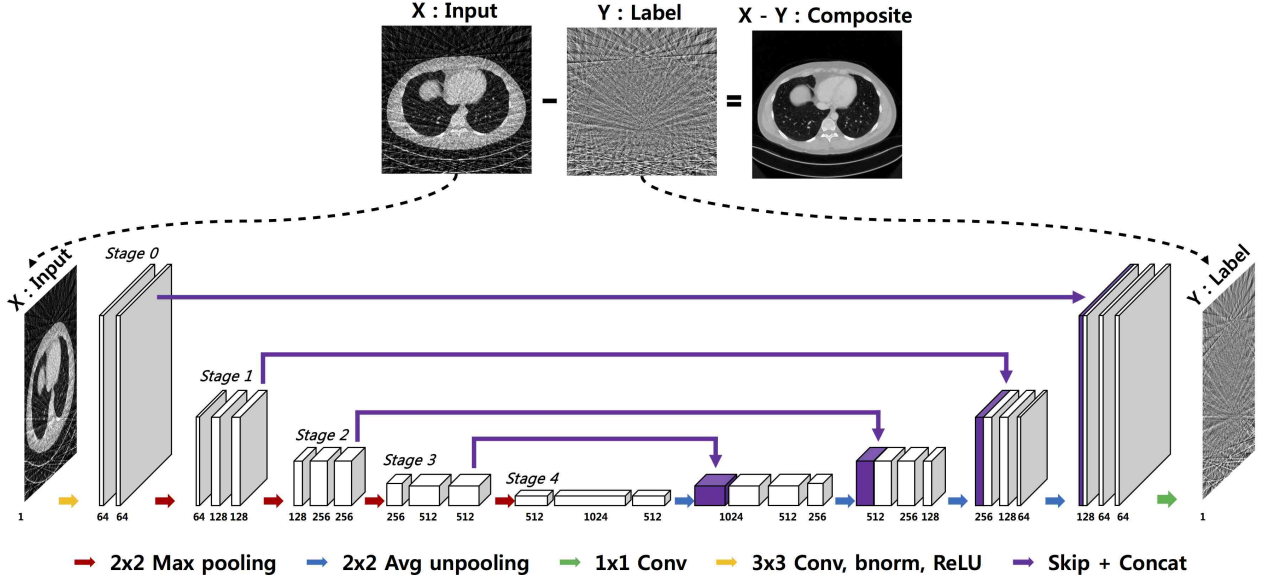


Figure 1. The proposed deep residual learning architecture for sparse view CT reconstruction.

mentation, we investigate several architectures of residual learning, which consistently shows that residual learning is better than image learning. In addition, among various residual learning architecture, we show that multi-scale deconvolution network with contracting path - which is often called U-net structure [15] for image segmentation - is most effective in removing streaking artifacts especially from very sparse number of projection views.

Contribution: In summary, our contributions are as following. First, a computational topology tool called the persistent homology is proposed as a novel tool to analyze the manifold of the label data. The analysis clearly shows the advantages of the residual learning in sparse view CT reconstruction. Second, among various type of residual learning architecture, multi-scale architecture known as U-net is shown the most effective. We show that the advantage of this architecture is originated from its enlarged receptive fields that can easily capture globally distributed artifact patterns. Finally, to our best knowledge, the proposed algorithm is the first deep learning architecture that successfully reconstruct high resolution images from very sparse number of projection views. Moreover, the proposed method significantly outperforms the existing compressed sensing CT approach in both image quality and reconstruction speed.

2. Related works

In CT reconstruction, only a few deep learning architectures are available. Kang *et al.* [7] provided the first systematic study of deep CNN in low-dose CT from reduced X-ray tube currents and showed that a deep CNN using directional wavelets is more efficient in removing low-dose related CT noises. Unlike these low-dose artifacts origi-

nated from reduced tube current, the streaking artifacts from sparse projection views exhibit globalized artifact patterns, which is difficult to remove using conventional denoising CNNs [4, 12, 20]. Therefore, to our best knowledge, there exists no deep learning architecture for sparse view CT reconstruction.

The residual learning concept was first introduced by He *et al.* [8] for image recognition. In low-level computer vision problems, Kim *et al.* [10] employed a residual learning for a super-resolution (SR) method. In these approaches, the residual learning was implemented by a skipped connection corresponding to an identity mapping. Unlike these architectures, Zhang *et al.* [21] proposed a direct residual learning architecture for image denoising and super-resolution, which has inspired our method.

The proposed architecture in Fig. 1 is originated from U-Net developed by Ronneberger *et al.* [15] for image segmentation. This architecture was motivated from another deconvolution network for image segmentation by Noh *et al.* [13] by adding contracting path and pooling/unpooling layers. However, we are not aware of any prior work that employed this architecture beyond the image segmentation.

3. Theoretical backgrounds

Before we explain the proposed deep residual learning architecture, this section provides theoretical backgrounds.

3.1. Generalization bound

In a learning problem, based on a random observation (input) $X \in \mathcal{X}$ and a label $Y \in \mathcal{Y}$ generated by a distribution D , we are interested in estimating a regression function $f : X \rightarrow Y$ in a functional space \mathcal{F} that mini-

mizes the risk $L(f) = E_D \|Y - f(X)\|^2$. A major technical issue is that the associated probability distribution D is unknown. Moreover, we only have a finite sequence of independent and identically distributed training data $S = \{(X_1, Y_1), \dots, (X_n, Y_n)\}$ such that only an empirical risk $\hat{L}_n(f) = \frac{1}{n} \sum_{i=1}^n \|Y_i - f(X_i)\|^2$ is available. Direct minimization of empirical risk is, however, problematic due to the overfitting.

To address these issues, statistical learning theory [1] has been developed to bound the risk of a learning algorithm in terms of complexity measures (eg. VC dimension and shatter coefficients) and the empirical risk. Rademacher complexity [2] is one of the most modern notions of complexity that is distribution dependent and defined for any class of real-valued functions. Specifically, with probability $\geq 1 - \delta$, for every function $f \in \mathcal{F}$,

$$L(f) \leq \underbrace{\hat{L}_n(f)}_{\text{empirical risk}} + \underbrace{2\hat{R}_n(\mathcal{F})}_{\text{complexity penalty}} + 3\sqrt{\frac{\ln(2/\delta)}{n}} \quad (1)$$

where the empirical Rademacher complexity $\hat{R}_n(\mathcal{F})$ is defined to be

$$\hat{R}_n(\mathcal{F}) = E_\sigma \left[\sum_{f \in \mathcal{F}} \left(\frac{1}{n} \sum_{i=1}^n \sigma_i f(X_i) \right) \right],$$

where $\sigma_1, \dots, \sigma_n$ are independent random variables uniformly chosen from $\{-1, 1\}$. Therefore, to reduce the risk, we need to minimize both the empirical risk (i.e. data fidelity) and the complexity term in (1) simultaneously.

In neural network, empirical risk is determined by the representation power of a network [18], whereas the complexity term is determined by the structure of a network. Furthermore, it was shown that the capacity of implementable functions grows exponentially with respect to the number of hidden units [14, 18]. Once the network architecture is determined, its capacity is fixed. Therefore, the performance of the network is now dependent on the complexity of the manifold of label Y that a given deep network tries to approximate.

In the following, using the persistent homology analysis, we show that the residual manifold composed of X-ray CT streaking artifacts is topologically simpler than the original one.

3.2. Manifold of CT streaking artifacts

In order to describe the manifold of CT streaking artifacts, this section starts with a brief introduction of CT physics and its analytic reconstruction method. For simplicity, a parallel-beam CT system is described. In CT, an X-ray photon undergoes attenuation according to Beers-Lambert law while it passes through the body. Mathematically, this

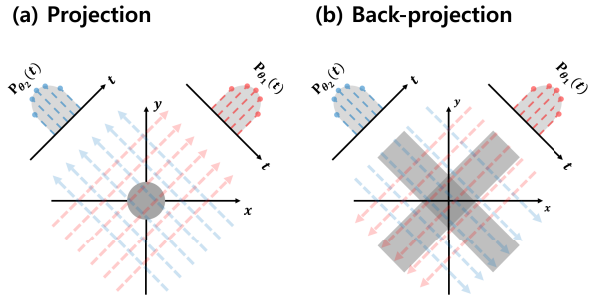


Figure 2. CT projection and back-projection operation.

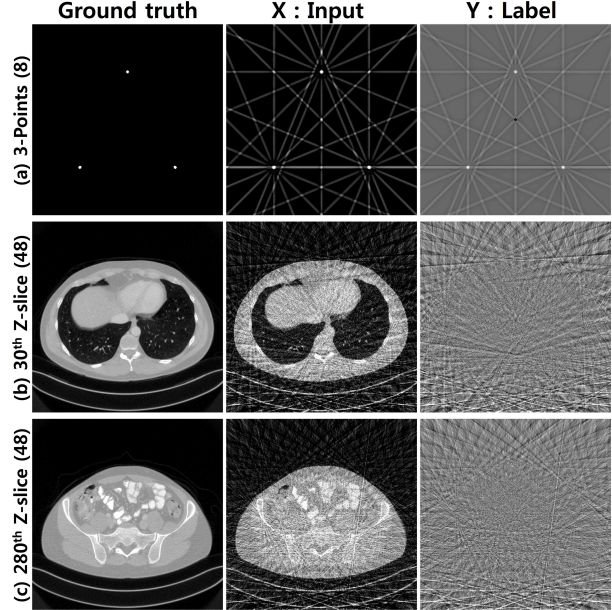


Figure 3. CT streaking artifact patterns for (a) three point targets from 8 view projection measurements and (b)(c) reconstruction images from 48 projections.

can be described by a Radon transform. Specifically, the projection measurement at the detector distance t in the projection angle θ is described by

$$P_\theta(t) = \int_{-\infty}^{\infty} \int_{-\infty}^{\infty} f(x, y) \delta(t - x \cos \theta - y \sin \theta) dx dy,$$

where $f(x, y)$ denotes the underlying image, and $t = x \cos \theta + y \sin \theta$ denotes the X-ray propagation path as shown in Fig. 2(a). If densely sampled projection measurements are available, the filtered back-projection (FBP)

$$f(x, y) = \int_0^\pi d\theta \int_{-\infty}^{\infty} |\omega| P_\theta(\omega) e^{j2\pi\omega t} d\omega, \quad (2)$$

becomes the inverse Radon transform, where $|\omega|$ denotes ramp filter and $P_\theta(\omega)$ indicates 1-D Fourier transform of projection along the detector t .

In (2), the outer integral corresponds to the back-projection that projects the filtered sinogram back along the

original X-ray beam propagation direction (see Fig. 2(b)). Accordingly, if the number of projection view is not sufficient, this introduces streaking artifacts. Fig. 3(a) shows a FBP reconstruction result from eight view projection measurements for three point targets. There exist significantly many streaking artifacts radiating from each point target. Fig. 3(b)(c) show two reconstruction images and their artifact-only images when only 48 projection views are available. Even though the underlying images are very different from the point targets and from each other, similar streaking artifacts radiating from objects are consistently observed. This suggests that the streaking artifacts from different objects may have similar topological structures.

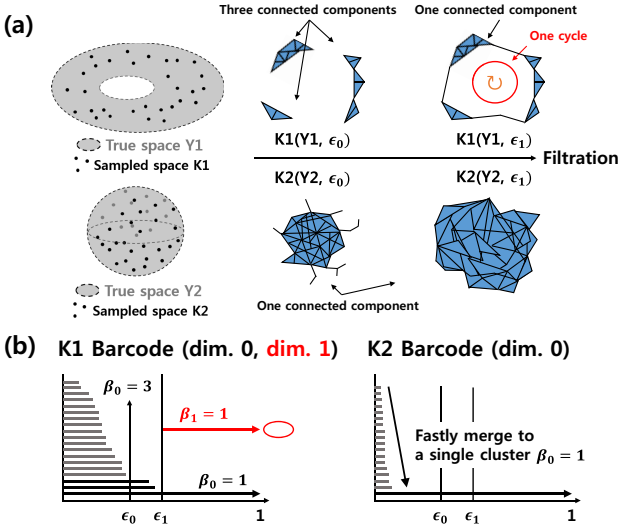


Figure 4. (a) Point cloud data K of true space Y and its configuration over ϵ distance filtration. Y_1 is a doughnut and Y_2 is a sphere shaped space each of which represents a complicated space and a simpler space, respectively. (b) Zero and one dimensional barcodes of K_1 and K_2 . Betti number can be easily calculated by counting the number of barcodes at each filtration value ϵ .

The complexity of a manifold is a topological concept. Thus, it should be analyzed using topological tools. In algebraic topology, Betti numbers (β_m) represent the number of m -dimensional holes of a manifold. For example, β_0 and β_1 are the number of connected components and cycles, respectively. They are frequently used to investigate the characteristic of underlying data manifold [6]. Specifically, we can infer the topology of a data manifold by varying the similarity measure between the data points and tracking the changes of Betti numbers. As allowable distance ϵ increases, point clouds merge together and finally become a single cluster. Therefore, the point clouds with high diversity will merge slowly and this will be represented as a slow decrease in Betti numbers. For example, in Fig. 4(a), the space Y_1 is a doughnut with a hole (i.e. $\beta_0 = 1$ and $\beta_1 = 1$) whereas Y_2 is a sphere-like cluster (i.e. $\beta_0 = 1$ and

$\beta_1 = 0$). Accordingly, Y_1 has longer zero dimensional *barcodes* persisting over ϵ in Fig. 4(b). In other words, it has a persisting one dimensional barcode implying the distanced configuration of point clouds that cannot be overcome until they reach a large ϵ . This persistence of Betti number is an important topological characteristics, and the recent *persistent homology* analysis utilizes this to investigate the topology of data [6].

In Bianchini *et al.* [3], Betti number of the set of inputs scored with a nonnegative response was used as a capacity measure of a deep neural network. However, our approach is novel, because we are interested in investigating the complexity of the label manifold. As will be shown in Experiment, the persistent homology analysis clearly show that the residual manifold has much simpler topology than the original one.

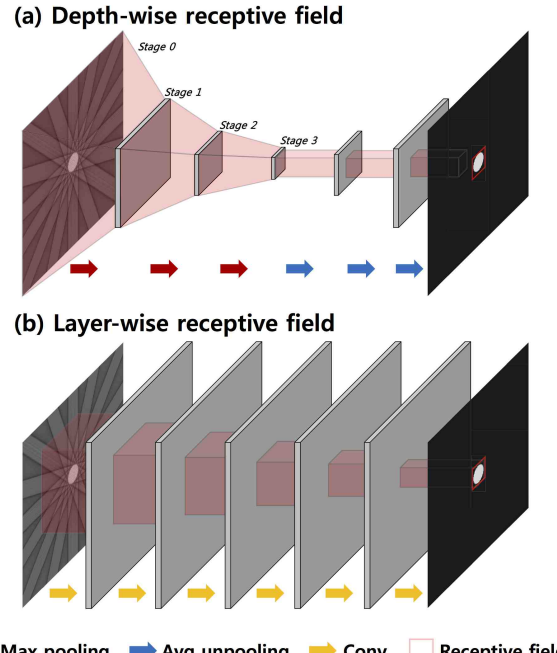


Figure 5. Effective receptive field comparison.

4. Residual Learning Architecture

As shown in Fig. 1, the proposed residual network consists of convolution layer, batch normalization [9], rectified linear unit (ReLU) [11], and contracting path connection with concatenation [15]. Specifically, each stage contains four sequential layers composed of convolution with 3×3 kernels, batch normalization, and ReLU layers. Finally, the last stage has two sequential layers and the last layer contains only one convolution layer with 1×1 kernel. In the first half of the network, each stage is followed by a max pooling layer, whereas an average unpooling layer is used in the later half of the network. Scale-by-scale contracting

paths are used to concatenate the results from the front part of the network to the later part of network. The number of channels for each convolution layer is illustrated in Fig. 1. Note that the number of channels are doubled after each pooling layers.

Fig. 5 compares the network depth-wise effective receptive field for a simplified form of the proposed network and a reference network without pooling layer. With the same convolutional filter, the effective receptive field is enlarged in the proposed architecture. Considering that the streaking artifact has globally distributed pattern as illustrated in Fig. 3, the enlarged effective receptive field from the multi-scale residual learning is more advantageous in removal of the streaking artifacts.

5. Experimental Results

5.1. Data Set

As a training data, we used the nine patient data provided by AAPM Low Dose CT Grand Challenge (<http://www.aapm.org/GrandChallenge/LowDoseCT/>). The data is composed of 3-D CT projection data from 2304 views. Artifact-free original images were generated by FBP using all 2304 projection views. Sparse view CT reconstruction input images X were generated using FBP from 48, 64, 96, and 192 projection views, respectively. For the proposed residual learning, the label data Y were defined as the difference between the sparse view reconstruction and the full-view reconstruction.

Among the nine patient data, eight patient data were used for training, whereas a test was conducted using the remaining one patient data. This corresponding to 3602 slices of 512×512 images for the training data, and 488 slices of 512×512 images for the test data. The training data was augmented by conducting horizontal and vertical flipping. For the training data set, we used the FBP reconstruction using both 48 and 96 projection views as input X and the difference between the full-view (2304views) reconstruction and the sparse view reconstructions were used as label Y .

Original vs. Residual

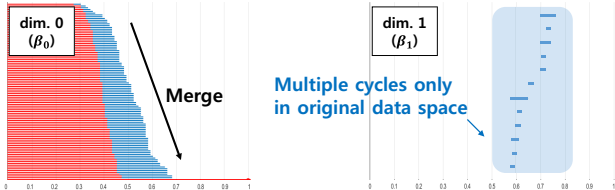


Figure 6. Zero and one dimensional barcodes of the artifact-free original CT images (blue) and streaking artifacts (red).

5.2. Persistent homology analysis

To compare the topology of the original and residual image spaces, we calculated Betti numbers using a toolbox called JAVAPLEX (<http://appliedtopology.github.io/javaplex/>). Each label image of size 512×512 was set to a point in \mathbb{R}^{512^2} vector space to generate a point cloud. We calculated Euclidean distance between each point and normalized it by the maximum distance. The topological complexity of both image spaces was compared by the change of Betti numbers in Fig. 6, which clearly showed that the manifold of the residual images are topologically simpler. Indeed, β_0 of residual image manifold decreased faster to a single cluster. Moreover, there exists no β_1 barcode for the residual manifold which infers a closely distributed point clouds as spherical example in Fig. 4(a)(b). These results clearly informs that the residual image manifold has a simpler topology than the original one.

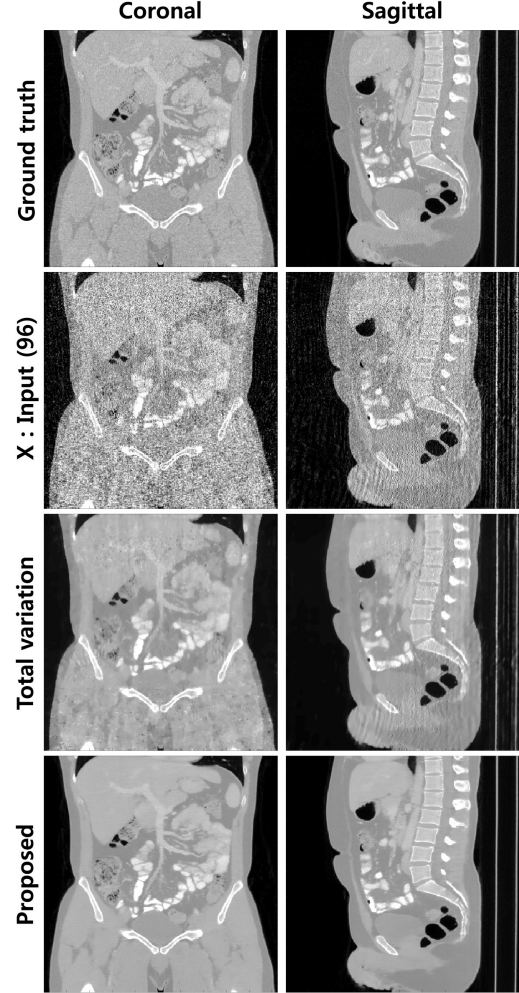


Figure 7. Reconstruction results by TV based compressed sensing CT, and the proposed method.

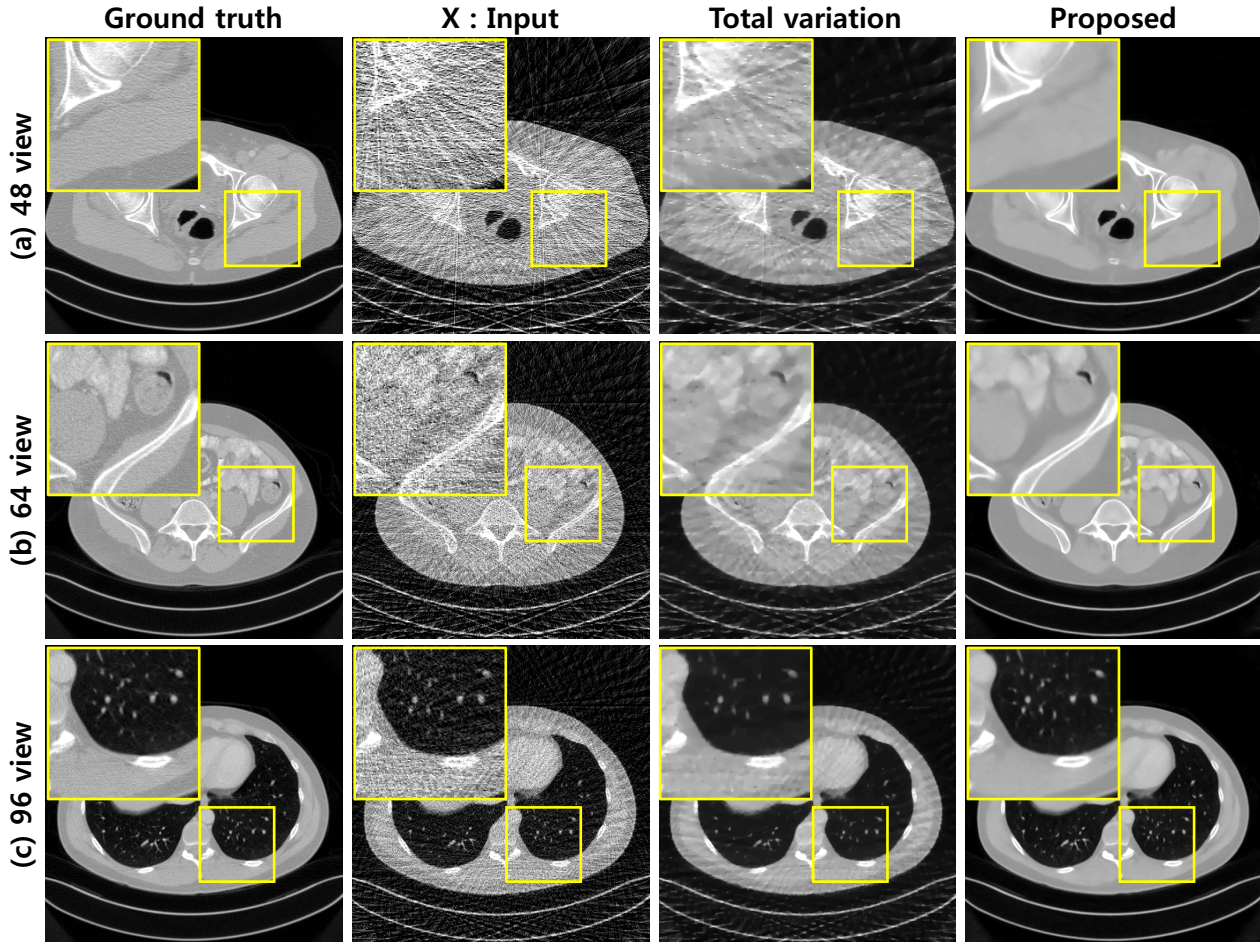


Figure 8. Axial view reconstruction results by TV based compressed sensing CT, and the proposed method.

5.3. Network training

The proposed network was trained by stochastic gradient descent (SGD). The regularization parameter was $\lambda = 10^{-4}$. The learning rate was set from 10^{-3} to 10^{-5} which was gradually reduced at each epoch. The number of epoch was 150. A mini-batch data using image patch was used, and the size of image patch was 256×256 .

The network was implemented using MatConvNet toolbox (ver.20) [19] in MATLAB 2015a environment (MathWorks, Natick). We used a GTX 1080 graphic processor and i7-4770 CPU (3.40GHz). The network takes about 1 day for training.

5.4. Reconstruction results

Fig. 7 shows reconstruction results from coronal and sagittal directions. Accurate reconstruction was obtained using the proposed method, whereas there exist remaining patterned artifacts in TV reconstruction. Fig. 8(a)-(c) shows the reconstruction results from axial views the proposed methods from 48, 64, and 96 projection views, respectively.

Note that the same network was used for all these cases to verify the universality of the proposed method. The results in Fig. 8(a)-(c) clearly showed that the proposed network removes most of streaking artifact patterns and preserves a detailed structure of underlying images. The magnified view in Fig. 8(a)-(c) confirmed that the detailed structures are very well reconstructed using the proposed method. Moreover, compared to the standard compressed sensing CT approach with TV penalty, the proposed results in Fig. 7 and Fig. 8 provides significantly improved image reconstruction results, even though the computational time for the proposed method is 123ms/slice. This is 30 time faster than the TV approach where the standard TV approach took about 3 ~ 4 sec/slice for reconstruction.

6. Discussion

6.1. Residual learning vs. Image learning

Here, we conduct various comparative studies. First, we investigated the importance of the residual learning. As for reference, an image learning network in Fig. 9(a) was used.

Although this has the same U-net structure as the proposed residual learning network in Fig. 1, the full view reconstruction results were used as label and the network was trained to learn the artifact-free images. According to our persistent homology analysis, the manifold of full-view reconstruction is topologically more complex so that the learning the full view reconstruction images is more difficult.

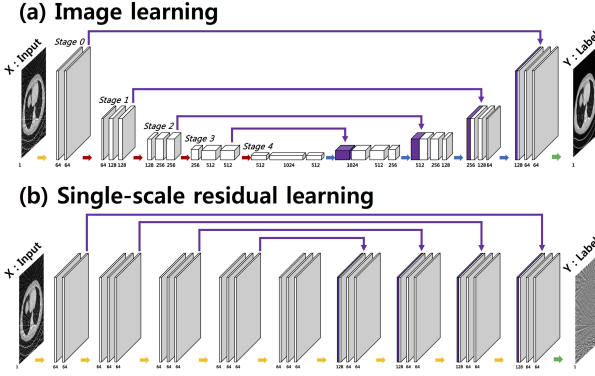


Figure 9. Reference networks.

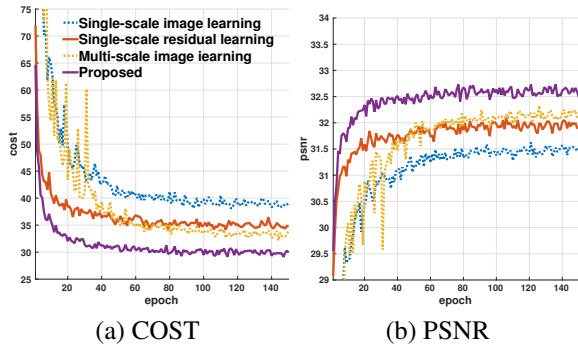


Figure 10. Convergence plots for (a) cost function, and (b) peak-signal-to-noise ratio (PSNR) with respect to each epoch.

The convergence plot in Fig. 10 and reconstruction results in Fig. 11 clearly show the strength of the residual learning over the image learning. The proposed residual learning network exhibits the fast convergence during the training and the final performance outperforms the image learning network. The magnified view of a reconstructed image in Fig. 11 clearly shows that the detailed structure of internal organ was not fully recovered using image learning, whereas the proposed residual learning can recover.

6.2. Single-scale vs. Multi-scale residual learning

Next, we investigated the importance of the multi-scale nature of residual learning using U-net. As for reference, a single-scale residual learning network as shown in Fig. 9(b) was used. Similar to the proposed method, the streaking artifact images were used as the labels. However, the resid-

ual network was constructed without pooling and unpooling layers. For fair comparison, we set the number of network parameters similar to the proposed method by fixing the number of channels at each layer across all the stages.

Fig. 10 clearly shows the advantages of multi-scale residual learning over single-scale residual learning. The proposed residual learning network exhibits the fast convergence and the final performance was better. In Fig. 12, the image reconstruction quality by the multi-scale learning was much improved compared to the single resolution one.

PSNR is shown as the quantification factor Table. 1. Here, in extremely sparse projection views, multi-scale structures always win the single-scale residual learning. At 192 projection views, the global streaking artifacts become less dominant compared to the localized artifacts, so the single-scale residual learning started to become better than multi-scale *image* learning approaches. However, by combining the advantages of residual learning and multi-scale network, the proposed multi-scale residual learning outperforms all the reference architectures in various view down-sampling ranges.

6.3. Diversity of training set

Fig. 13 shows that reconstructed results by the proposed approach, when the network was trained with sparse view reconstruction from 48, 96, or 48 and 96 views, respectively. The streaking artifacts were removed very well in all cases; however, the detailed structure of underlying image was maintained when the network was trained using 96 view reconstruction, especially when the network was used to reconstruct image from more dense view data set (198 views in this case). On the other hand, the network trained with 96 views could not be used for 48 views sparse CT reconstruction. Fig. 13 clearly showed the remaining streaking artifact in this case.

To address this issue and make the network universal across wide ranges of view down-sampling, the proposed network was, therefore, trained using a training data set by combining sparse CT reconstruction data between 48 and 96 view. As shown in Fig. 13, the proposed approach with the combined training provided the best reconstruction across wide ranges of view down-sampling.

7. Conclusion

In this paper, we develop a novel deep residual learning approach for sparse view CT reconstruction. Based on the persistent homology analysis, we showed that the residual manifold composed of streaking artifacts is topologically simpler than the original one. This claim was confirmed using persistent homology analysis and experimental results, which clearly showed the advantages of the residual learning over image learning. Among the various residual learning networks, this paper showed that the multi-scale resid-

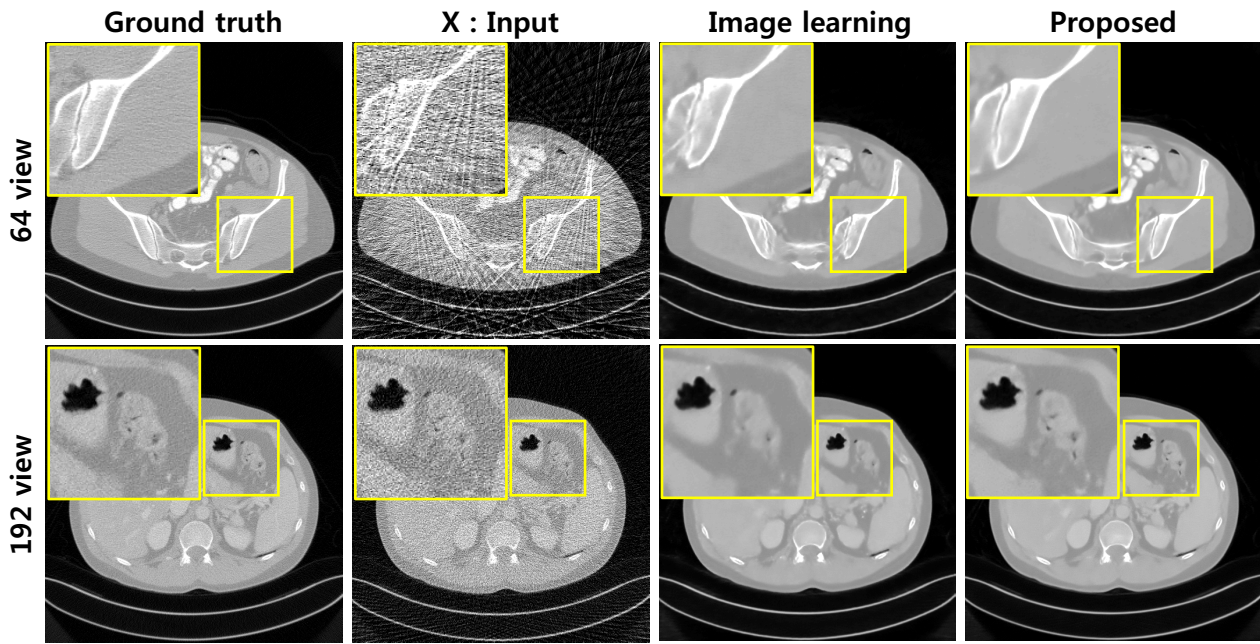


Figure 11. Comparison results for residual learning and image learning from 64 and 192 view reconstruction input data.

No. of views	Single-scale image learning	Single-scale residual learning	Multi-scale image learning	Proposed
48 view	31.0027	31.7550	32.5525	33.3916
64 view	32.1380	32.4456	32.9748	33.8680
96 view	33.2983	33.3569	33.4728	34.5898
192 view	33.7693	33.8390	33.7101	34.9028

Table 1. Average PSNR results for various learning architectures.

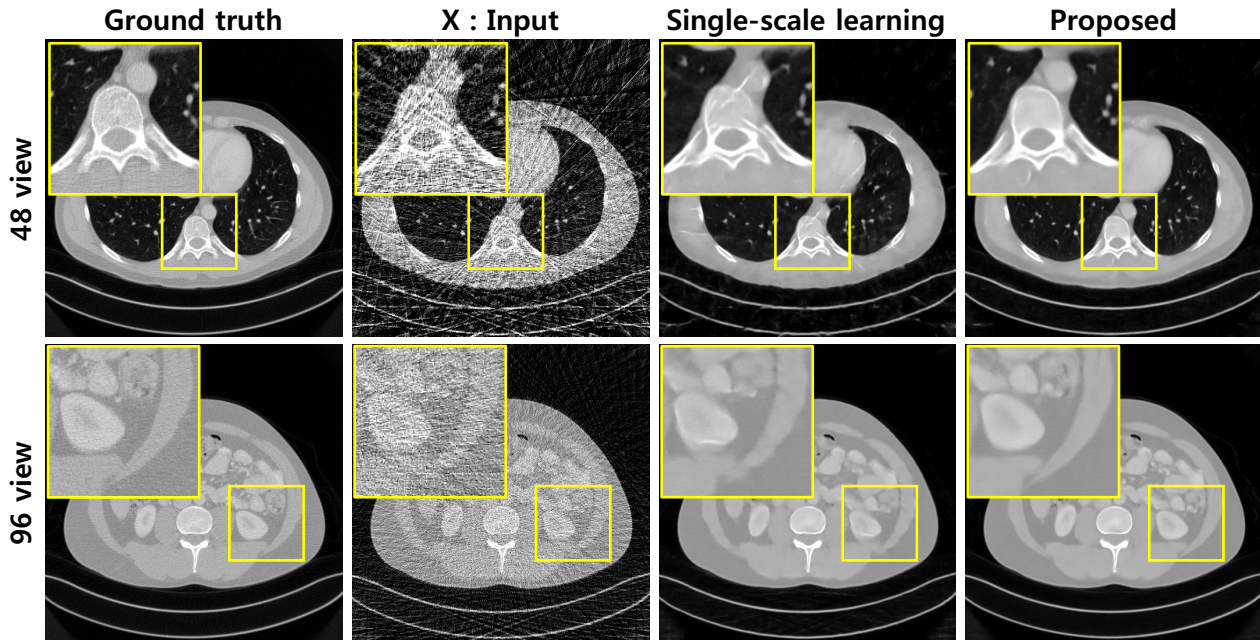


Figure 12. Comparison results for single-scale versus multi-scale residual learning from 48 and 96 view reconstruction input data.

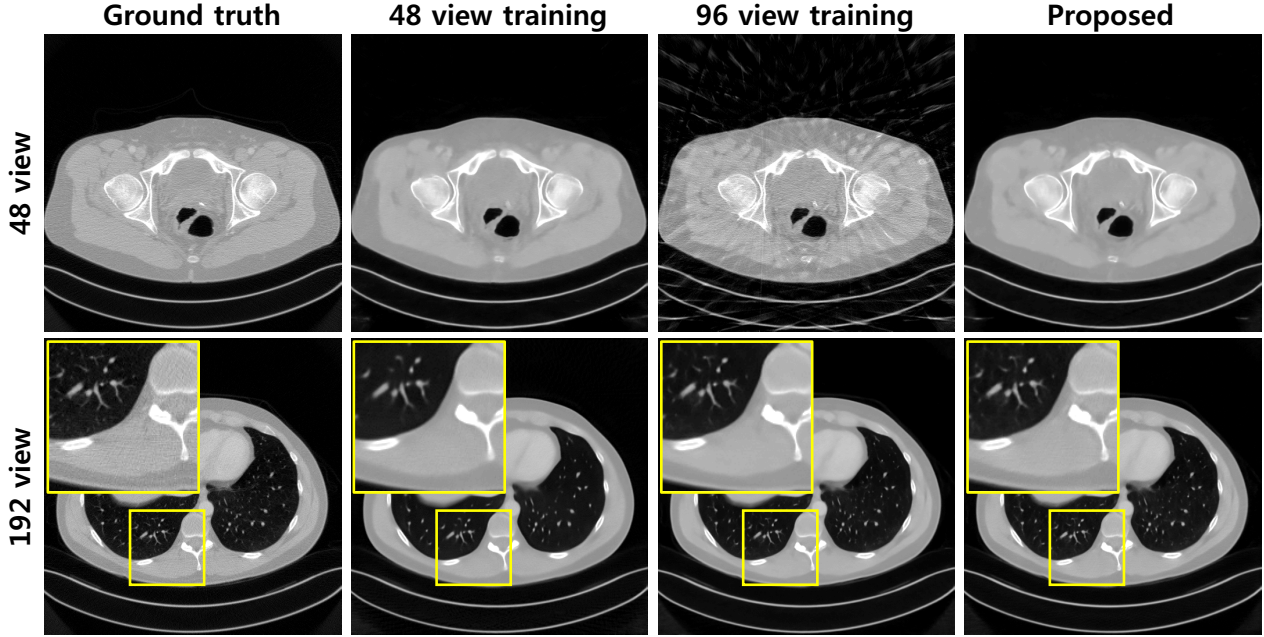


Figure 13. Comparison results for various training data configuration. Each column represents reconstructed images by proposed network which was trained with sparse view reconstruction from 48, 96, or 48/96 views, respectively.

ual learning using U-net structure was the most effective especially when the number of views were extremely small. We showed that this is due to the enlarged receptive field in U-net structure that can easily capture the globally distributed streaking artifacts. Using extensive experiments, we showed that the proposed deep residual learning is significantly better than the conventional compressed sensing CT approaches. Moreover, the computational speed was extremely faster than that of compressed sensing CT.

Although this work was mainly developed for sparse view CT reconstruction problems, the proposed residual learning network may be universally used for removing various image noise and artifacts that are globally distributed.

8. Acknowledgement

The authors would like to thanks Dr. Cynthia McCollough, the Mayo Clinic, the American Association of Physicists in Medicine (AAPM), and grant EB01705 and EB01785 from the National Institute of Biomedical Imaging and Bioengineering for providing the Low-Dose CT Grand Challenge data set. This work is supported by Korea Science and Engineering Foundation, Grant number NRF-2016R1A2B3008104.

References

- [1] M. Anthony and P. L. Bartlett. *Neural network learning: Theoretical foundations*. cambridge university press, 2009. [1](#) [3](#)
- [2] P. L. Bartlett and S. Mendelson. Rademacher and Gaussian complexities: Risk bounds and structural results. *Journal of Machine Learning Research*, 3(Nov):463–482, 2002. [1](#) [3](#)
- [3] M. Bianchini and F. Scarselli. On the complexity of neural network classifiers: A comparison between shallow and deep architectures. *IEEE Trans. on Neural Networks and Learning Systems*, 25(8):1553–1565, 2014. [4](#)
- [4] Y. Chen, W. Yu, and T. Pock. On learning optimized reaction diffusion processes for effective image restoration. In *Proceedings of the IEEE Conference on Computer Vision and Pattern Recognition*, pages 5261–5269, 2015. [2](#)
- [5] D. L. Donoho. Compressed sensing. *IEEE Transactions on information theory*, 52(4):1289–1306, 2006. [1](#)
- [6] H. Edelsbrunner and J. Harer. Persistent homology—a survey. *Contemporary mathematics*, 453:257–282, 2008. [1](#) [4](#)
- [7] K. Eunhee, M. Junhong, and Y. Jong Chul. A deep convolutional neural network using directional wavelets for low-dose x-ray ct reconstruction. *arXiv preprint arXiv:1610.09736*, 2016. [2](#)
- [8] K. He, X. Zhang, S. Ren, and J. Sun. Deep residual learning for image recognition. *arXiv preprint arXiv:1512.03385*, 2015. [2](#)

- [9] S. Ioffe and C. Szegedy. Batch normalization: Accelerating deep network training by reducing internal covariate shift. *arXiv preprint arXiv:1502.03167*, 2015. 4
- [10] J. Kim, J. K. Lee, and K. M. Lee. Accurate image super-resolution using very deep convolutional networks. *arXiv preprint arXiv:1511.04587*, 2015. 1, 2
- [11] A. Krizhevsky, I. Sutskever, and G. E. Hinton. Imagenet classification with deep convolutional neural networks. In *Advances in neural information processing systems*, pages 1097–1105, 2012. 1, 4
- [12] X.-J. Mao, C. Shen, and Y.-B. Yang. Image denoising using very deep fully convolutional encoder-decoder networks with symmetric skip connections. *arXiv preprint arXiv:1603.09056*, 2016. 2
- [13] H. Noh, S. Hong, and B. Han. Learning deconvolution network for semantic segmentation. In *Proceedings of the IEEE International Conference on Computer Vision*, pages 1520–1528, 2015. 2
- [14] B. Poole, S. Lahiri, M. Raghu, J. Sohl-Dickstein, and S. Ganguli. Exponential expressivity in deep neural networks through transient chaos. *arXiv preprint arXiv:1606.05340*, 2016. 1, 3
- [15] O. Ronneberger, P. Fischer, and T. Brox. U-net: Convolutional networks for biomedical image segmentation. In *International Conference on Medical Image Computing and Computer-Assisted Intervention*, pages 234–241. Springer, 2015. 1, 2, 4
- [16] W. Shi, J. Caballero, F. Huszár, J. Totz, A. P. Aitken, R. Bishop, D. Rueckert, and Z. Wang. Real-time single image and video super-resolution using an efficient sub-pixel convolutional neural network. In *Proceedings of the IEEE Conference on Computer Vision and Pattern Recognition*, pages 1874–1883, 2016. 1
- [17] E. Y. Sidky and X. Pan. Image reconstruction in circular cone-beam computed tomography by constrained, total-variation minimization. *Physics in medicine and biology*, 53(17):4777, 2008. 1
- [18] M. Telgarsky. Benefits of depth in neural networks. *arXiv preprint arXiv:1602.04485*, 2016. 1, 3
- [19] A. Vedaldi and K. Lenc. Matconvnet: Convolutional neural networks for matlab. In *Proceedings of the 23rd ACM international conference on Multimedia*, pages 689–692. ACM, 2015. 6
- [20] J. Xie, L. Xu, and E. Chen. Image denoising and inpainting with deep neural networks. In *Advances in Neural Information Processing Systems*, pages 341–349, 2012. 2
- [21] K. Zhang, W. Zuo, Y. Chen, D. Meng, and L. Zhang. Beyond a gaussian denoiser: Residual learning of deep cnn for image denoising. *arXiv preprint arXiv:1608.03981*, 2016. 1, 2